



# Meridional Ocean Carbon Transport

Aitor Aldama-Campino<sup>1,2</sup>, Filippa Fransner<sup>3</sup>, Malin Ödalen<sup>1,2,4</sup>, Sjoerd

Groeskamp<sup>5</sup>, Andrew Yool<sup>6</sup>, Kristofer Döös<sup>1,2</sup>, Jonas Nylander<sup>1,2</sup>

<sup>1</sup>Department of Meteorology, Stockholm University, Sweden

<sup>2</sup>Bolin Centre for Climate Research, Stockholm University, Sweden

<sup>3</sup>Geophysical Institute, University of Bergen, and Bjerknes Centre for Climate Research, Bergen, Norway

<sup>4</sup>Department of Geosciences, University of Arizona, USA

<sup>5</sup>NIOZ Royal Netherlands Institute for Sea Research, Department of Ocean Systems, and Utrecht

University, Texel, the Netherlands

<sup>6</sup>National Oceanography Centre, European Way, Southampton, United Kingdom

## Key Points:

- The redistribution of DIC by ocean meridional circulation is quantified and related to physical and biological processes.
- Transports of solubility carbon dominates the upper ocean and the NADW, biogenic carbon the deep ocean.
- Pacific biological pump is the most important process retaining carbon on longer time scales.

Corresponding author: Aitor Aldama-Campino, [aitor.alldama@outlook.com](mailto:aitor.alldama@outlook.com)

This article has been accepted for publication and undergone full peer review but has not been through the copyediting, typesetting, pagination and proofreading process which may lead to differences between this version and the Version of Record. Please cite this article as doi: [10.1029/2019GB006336](https://doi.org/10.1029/2019GB006336)

**18 Abstract**

19 The ocean's ability to take up and store CO<sub>2</sub> is a key factor for understanding past and  
20 future climate variability. However, qualitative and quantitative understanding of surface-  
21 to-interior pathways, and how the ocean circulation affects the CO<sub>2</sub> uptake, is limited.  
22 Consequently, how changes in ocean circulation may influence carbon uptake and stor-  
23 age and therefore the future climate remains ambiguous.

24 Here we quantify the roles played by ocean circulation and various water masses  
25 in the meridional redistribution of carbon. We do so by calculating streamfunctions de-  
26 fined in Dissolved Inorganic Carbon (DIC) and latitude coordinates, using output from  
27 a coupled biogeochemical-physical model. By further separating DIC into components  
28 originating from the solubility pump and a residual including the biological pump, air-  
29 sea disequilibrium and anthropogenic CO<sub>2</sub>, we are able to distinguish the dominant path-  
30 ways of how carbon enters particular water masses.

31 With this new tool, we show that the largest meridional carbon transport occurs  
32 in a pole-to-equator transport in the subtropical gyres in the upper ocean. We are able  
33 to show that this pole-to-equator DIC transport, and the Atlantic Meridional Overturn-  
34 ing Circulation (AMOC) related DIC transport, are mainly driven by the solubility pump.  
35 By contrast, the DIC transport associated with deep circulation, including that in Antarc-  
36 tic Bottom Water and Pacific Deep Water, is mostly driven by the biological pump. As  
37 these two pumps, as well as ocean circulation, are widely expected to be impacted by  
38 anthropogenic changes, these findings have implications for the future role of the ocean  
39 as a climate-buffering carbon reservoir.

**40 1 Introduction**

41 The ocean circulation and its redistribution of carbon are important parts of the  
42 global carbon cycle and have significant impacts on the atmospheric pCO<sub>2</sub> (Sabine et  
43 al., 2004; Caias et al., 2013; Sarmiento & Gruber, 2006; Mikaloff Fletcher et al., 2007).  
44 With rising atmospheric pCO<sub>2</sub> and related climate change, many studies have focused  
45 on air-sea CO<sub>2</sub> exchange (e.g. Takahashi et al. (2002); Le Quéré et al. (2007); Landschützer  
46 et al. (2015); Yasunaka et al. (2018)), and how the physical and biological pumps drive  
47 the air-sea exchange (Volk & Hoffert, 2013). How this air-sea CO<sub>2</sub> exchange connects  
48 the surface to the ocean interior via large scale ocean circulation is, however, less well-

49 constrained (Levy et al., 2013). This is largely related to the difficulties in distinguishing  
50 the role of ocean water masses and circulation patterns in ocean carbon transport.

51 Estimates of meridional ocean carbon transport have been made through inverse  
52 calculations based on observed air-sea CO<sub>2</sub> exchange and its variations (Gloor et al., 2003;  
53 Mikaloff Fletcher et al., 2007; Gruber et al., 2009). These do not, however, give any in-  
54 formation on the control that the various circulation cells exerts on carbon transport and  
55 redistribution within the ocean. Meridional carbon transport has also been calculated  
56 by the product of volume flow and carbon concentrations (Brewer et al., 1989; W. Broecker  
57 & Peng, 1992), which gives a rough estimate, but does not give a global view. Iudicone  
58 et al. (2011) made a detailed analysis of the role of separate water masses in the trans-  
59 ports of carbon in and out of the Southern Ocean. Studies such as these provide an im-  
60 portant basis for our knowledge of overall ocean carbon transports. However, they do  
61 not explain how the transport is connected globally, nor do they clarify the sources of  
62 the transported carbon, i.e. whether it originates from the physical or the biological pumps.

63 The physical – or solubility – pump is the mechanism by which carbon enters the  
64 deep ocean via sites of deep water formation (Volk & Hoffert, 1985). These sites trans-  
65 fer dense seawater into the ocean interior, typically at high latitudes, where cooler sur-  
66 face temperatures enhance the solubility of CO<sub>2</sub>. Consequently, waters reaching the ocean  
67 interior have elevated concentrations of Dissolved Inorganic Carbon (DIC) driven by this  
68 physical mechanism. In contrast, the biological pump is ultimately driven by the pro-  
69 duction of organic matter (plus carbonate biominerals) by photosynthetic phytoplank-  
70 ton at the ocean’s surface (Volk & Hoffert, 1985). After processing through the foodweb,  
71 a fraction of this production is exported from the surface to the interior ocean by either  
72 gravitational sinking or subduction. Its remineralisation within the ocean liberates DIC,  
73 elevating water column concentrations through biological mechanisms.

74 The aim of this study is to present a diagnostic tool to estimate the global merid-  
75 ional transport of DIC related to ocean circulation cells in the ocean interior. It builds  
76 on Groeskamp et al. (2016), who developed a new method for calculating the transport  
77 of anthropogenic carbon to the ocean interior based on streamfunctions. Further, we link  
78 the origins of the transported carbon to the physical and biological ocean carbon pumps,  
79 which comprise the main pathways by which carbon enters the ocean interior. By do-  
80 ing this, we provide further clues to understanding the role of physical and biological ocean

processes in ocean carbon storage and, by inference, in regulating atmospheric pCO<sub>2</sub>. This method, which consists of a dimensional reduction of the system to a two dimensional projection, can be used for instance to simplify model intercomparisons or to identify notable changes in ocean carbon transport and identify the responsible processes.

## 2 Methods

### 2.1 Carbon decomposition

In the ocean, dissolved CO<sub>2</sub> exists in several different forms. About 90% exists as bicarbonate, 9% as carbonate, and a small fraction of the concentration is in the form of aqueous CO<sub>2</sub> and carbonic acid (Williams & Follows, 2011). Together, these species are commonly known as Dissolved Inorganic Carbon (DIC). The total ocean concentration of DIC will from now on be referred to as  $C_{tot}$ . Per Equation 1, it can be partitioned into contributions from different processes associated with the solubility pump and the biological pump (Eggleston & Galbraith, 2018; Ito & Follows, 2005; Ödalen et al., 2018; Williams & Follows, 2011). The partitioning allows us to quantify the contribution of solubility pump and biological pump processes to carbon transports in different water masses.

The solubility pump describes the pathway for carbon that enters the ocean via physico-chemical dissolution in the surface ocean. In our simulations, this consists of three components; saturation carbon ( $C_{sat}$ ), disequilibrium carbon ( $C_{dis}$ ) and anthropogenic carbon ( $C_{anth}$ ). In this paper, we focus mainly on  $C_{sat}$ , which is described in more detail below. The biological pump involves carbon that is biologically fixed in particulate material in the surface ocean and then transported (via gravitational sinking and circulation) to the deep ocean where it is remineralised back to DIC. We refer to this DIC as  $C_{bio}$ .

We apply the same ocean carbon partitioning framework as in Lauderdale et al. (2013), with the addition of a component associated with anthropogenic emissions (Couldrey, 2018):

$$C_{tot} = C_{sat} + C_{bio} + \underbrace{C_{dis} + C_{anth}}_{C_{res}} + \epsilon \quad (1)$$

Here, the  $\epsilon$  term represents any discrepancies associated with the computation methods in the solution of the carbon system equations (Lewis et al., 1998) and the compu-

110 tation of  $C_{bio}$  and its constituents (Lauderdale et al. (2013); McDougall and Barker (2011),  
111 see Supplementary Information).

112  $C_{sat}$ , the bulk of  $C_{tot}$  associated with the solubility pump, originates from CO<sub>2</sub> dis-  
113 solving in water until the water reaches saturation, for a constant reference atmospheric  
114 pCO<sub>2</sub> (henceforth pCO<sub>2</sub><sup>atm</sup>), at the ambient ocean temperature, alkalinity and salinity  
115 (see Section 2.3). Whenever water is not at saturation when it leaves the ocean surface,  
116 there is also a disequilibrium contribution to carbon ( $C_{dis}$ ), which can be positive or neg-  
117 ative. If pCO<sub>2</sub><sup>atm</sup> changes over time, for example through anthropogenic emissions, this  
118 contribution to ocean  $C_{tot}$  can be accounted for separately ( $C_{anth}$ ) (Couldrey, 2018). In  
119 this work, however, we do not study the separate contributions from  $C_{dis}$  and  $C_{anth}$ , so  
120 together with  $\epsilon$ , these are treated as a solubility pump residual ( $C_{res}$ , see Equation 1).

121  $C_{sat}$ ,  $C_{dis}$  and  $C_{anth}$  are so called preformed tracers, which are only modified at  
122 the ocean surface and act as passive tracers in the ocean interior.  $C_{bio}$  is equal to zero  
123 at the surface, but has local sources in the interior ocean. As  $C_{sat}$  acts as a conserved  
124 tracer in the interior ocean, we choose to study it separately. We also look at the remain-  
125 ing terms taken together ( $C_{bio+res}$ ) by subtracting the computed  $C_{sat}$  from  $C_{tot}$ :

$$C_{tot} - C_{sat} = C_{bio+res} \quad (2)$$

## 126 2.2 Meridional streamfunctions

### 127 2.2.1 Meridional overturning streamfunctions

128 Streamfunctions are a diagnostic tool often used in both atmospheric science and  
129 physical oceanography, which help to understand different processes such as volume trans-  
130 ports. The idea behind streamfunctions is a dimensional reduction of the system to a  
131 two-dimensional projection. The most traditional streamfunctions are based on two ge-  
132 ographical coordinates. For instance, the latitude-depth stream function  $\Psi(\phi_0, z_0)$ , usu-  
133 ally referred to as the meridional overturning stream function is, among the different set  
134 of streamfunctions, the most used and known one. The meridional overturning stream-  
135 function is given by the following equation:

$$\Psi(\phi_0, z_0) = \frac{1}{t_f - t_0} \int_{t_0}^{t_f} \int_{\Omega} \delta[\phi_0 - \phi] \mu[z_0 - z] v(\vec{x}, t) d\Omega dt \quad (3)$$

136 where  $\phi_0$  is the chosen latitude,  $z_0$  is the reference depth,  $v(\vec{x}, t)$  is the meridional ve-  
137 locity field (in m s<sup>-1</sup>),  $t_f$  and  $t_0$  represent the final and the initial time respectively (in

138 s), and  $\Omega$  represents the volume domain over which the streamfunction is computed. In  
 139 this particular case, where we are defining latitude  $\phi$  to describe the meridional coor-  
 140 dinate,  $d\Omega$  has area units ( $\text{m}^2$ ) and is given by  $d\Omega = d\phi \, dx \, dz$ . The units of the stream-  
 141 function are given in [ $\text{m}^3 \, \text{s}^{-1}$ ] (which represent a volume transport). For convenience,  
 142 however, the results will be presented in Sverdrups,  $1 \, \text{Sv} \equiv 10^6 \, \text{m}^3 \, \text{s}^{-1}$ .

143 By imposing both the Dirac delta pseudo-function  $\delta[\star]$  and the Heaviside's step func-  
 144 tion  $\mu[\star]$ , the stream function only considers the volume fluxes at  $\phi_0$  at depths equal or  
 145 below  $z_0$ . Therefore, this stream function represents the total average meridional mass  
 146 transport below a given depth value  $z_0$ , at a chosen latitude  $\phi_0$ . If there are no mass sources  
 147 or sinks, this value also represents the total vertical mass transport north of  $\phi_0$  at a depth  
 148  $z_0$ .

#### 149 ***2.2.2 A generalised meridional streamfunction***

150 The meridional overturning circulation can be generalised to any coordinate  $\xi$  which  
 151 could be another geographical coordinate (e.g. longitude as in the barotropic stream func-  
 152 tion), a thermodynamic coordinate (e.g. temperature), or as we will present in this work  
 153 a biogeochemical tracer. The generalised meridional streamfunctions is described by the  
 154 following equation:

$$\Psi(\phi_0, \xi_0) = \frac{1}{t_f - t_0} \int_{t_0}^{t_f} \int_{\Omega} \delta[\phi_0 - \phi] \mu[\xi_0 - \xi(\vec{x}, t)] v(\vec{x}, t) d\Omega \, dt \quad (4)$$

155 where  $\xi_0$  is the reference isoline value of the selected tracer (in this study  $C_{tot}$  and  $C_{sat}$ ).  
 156 A positive value of the streamfunction represents a net northward volume transport for  
 157 waters with a tracer value lower or equal to  $\xi_0$ .

158 There is a special set of streamfunctions where a proper choice of the coordinate  
 159  $\xi$  transforms the general meridional stream function into an extended version of the merid-  
 160 ional overturning circulation. In this case  $\xi$ , a non-geographical coordinate, behaves as  
 161 a pseudo-depth where its values can be related to a depth level. This relation facilitates  
 162 an estimate of the vertical position in the geographical space directly from the stream-  
 163 function in the  $\phi-\xi$  space. Nevertheless, it is possible to identify the overturning cells  
 164 that may arise from  $\Psi(\phi, \xi)$  in geographical space by locating them for a given latitude  
 165 and tracer value.

Moreover, the streamfunction can be computed for a particular basin by applying a mask function to the integral. In this study we have considered three basins: the Southern Ocean (covering all the water masses south of cape Agulhas, 34°S), the Atlantic Ocean (which includes the Mediterranean and Black Sea, and the Arctic Ocean), and the Indo-Pacific Ocean. Cape Agulhas is selected as the cut-off latitude to avoid splitting the Antarctic Circumpolar Current (ACC) into two different basins. However, this split cannot be applied to the tracer coordinate. For example, it is not possible to compute the associated streamfunction for  $C_{bio+res}$  by subtracting the  $C_{sat}$  streamfunction from the  $C_{tot}$  streamfunction. This is a result of the non-linearity of the step function inside the integral.

### 2.2.3 Meridional transports

In a non-divergent fluid the meridional transport of the tracer can be computed by integrating the streamfunction along the tracer space. However, the ocean is a divergent fluid as the evaporation, precipitation and river runoff act as sources or sinks at the surface. In order to minimise the effect of the divergence, we will introduce a reference tracer value  $\xi^R$ . The transport is given by:

$$Tr(\phi_0) = \int_{\xi_{min}}^{\xi_{max}} (\xi_0 - \xi^R) \frac{\partial \Psi(\phi_0, \xi_0)}{\partial \xi_0} d\xi_0 \quad (5)$$

In this study we chose the mean value of the tracer as  $\xi^R$ . The sensitivity to the choice of the reference value is discussed in Appendix B. Inserting the definition of the streamfunction we will obtain the following result:

$$\begin{aligned} Tr(\phi_0) &= \int_{\xi_{min}}^{\xi_{max}} (\xi_0 - \xi^R) \left( \frac{1}{t_f - t_0} \int_{t_0}^{t_f} \int_{\Omega} \delta[\phi_0 - \phi] \delta[\xi_0 - \xi(\vec{x}, t)] v(\vec{x}, t) d\Omega dt \right) d\xi_0 = \\ &= \frac{1}{t_f - t_0} \int_{t_0}^{t_f} \int_{\Omega} \delta[\phi_0 - \phi] \left( \int_{\xi_{min}}^{\xi_{max}} (\xi_0 - \xi^R) \delta[\xi_0 - \xi(\vec{x}, t)] d\xi_0 \right) v(\vec{x}, t) d\Omega dt \\ &= \frac{1}{t_f - t_0} \int_{t_0}^{t_f} \int_{\Omega} \delta[\phi_0 - \phi] (\xi(\vec{x}, t) - \xi^R) v(\vec{x}, t) d\Omega dt \end{aligned} \quad (6)$$

This recovers the traditional expression for a meridional transport of a tracer computed directly from the velocity and the tracer field. Most of the fields analysed in this study ( $C_{tot}$ ,  $C_{sat}$  and  $C_{bio+res}$ ) are positive definite, therefore, a positive value of the transport represents a northward transport of the tracer. A description on how to compute the streamfunction and the transports numerically can be found in Appendix A and Appendix B.

191        **2.3 Model data and analysis**

192        We use the output from a simulation of the coupled physical-biogeochemical model  
 193        NEMO-MEDUSA (Yool et al., 2015). NEMO (Madec, 2012) is used here in a global ORCA025  
 194        configuration, with a horizontal resolution of approximately  $0.25^\circ$  (an average grid cell  
 195        size of 19.0 km globally) and with 75 vertical levels (increasing in thickness from 1 m at  
 196        the surface to 200 m at 6000 m). This particular simulation has been run using NEMO  
 197        v3.4 with the LIM2 sea-ice model (Timmermann et al., 2005).

198        The biogeochemical model, MEDUSA-2 (Yool et al., 2013), is an intermediate com-  
 199        plexity framework containing a representation of the elemental cycles of nitrogen, car-  
 200        bon, oxygen, silicon and iron. The plankton ecosystem is comprised of dual size classes  
 201        of phytoplankton, zooplankton and detritus components. It is a nitrogen-based model,  
 202        with the biological transformations of other elemental cycles related to that of nitrogen  
 203        by fixed “Redfield” ratios (except silicon, which has a dynamic ratio).

204        The output used here is a 10 year period from 2000-2009, drawn from a run that  
 205        contains both historical and future simulations, as it is run for the period 1975-2099 (Yool  
 206        et al., 2015). The model was initialised in 1975 using physical and biogeochemical fields  
 207        from a lower horizontal resolution simulation (ORCA1;  $1^\circ$  horizontal resolution), run for  
 208        the period 1860-1975. This lower-resolution model was forced at its surface boundary  
 209        using atmospheric fields (including atmospheric  $p\text{CO}_2$ ) from a CMIP5 Historical sim-  
 210        ulation of the HadGEM2-ES model (Jones et al., 2011; Yool et al., 2015). The ORCA025  
 211        configuration continued with the same forcing regime from 1975 onwards. After 2005,  
 212        the simulation followed an IPCC climate projection using the Representative Concen-  
 213        tration Pathway (RCP) 8.5 scenario. This future projection describes a continuous in-  
 214        crease of greenhouse gas emission throughout the 21st century reaching a radiative forc-  
 215        ing of  $8.5 \text{ W m}^{-2}$  by the end of the century.

216        The saturation carbon,  $C_{sat}$ , was computed using the carbon system equations solver  
 217        CO2SYS (Lewis et al., 1998) by providing *in situ* temperature, salinity, global mean al-  
 218        kalinity and a reference  $p\text{CO}_2^{atm}$  based on the 1860 value (286 ppm). The climatolog-  
 219        ical cross sections of  $C_{tot}$  in the Atlantic ( $25^\circ\text{W}$ ) and Indo-Pacific ( $170^\circ\text{W}$ ) are computed  
 220        from the model output of the selected ten year time period (2000-2009; Figure 1). This  
 221        climatology is computed from the model output of the selected ten year time period (2000-  
 222        2009). In panels c and d, we show the corresponding computed  $C_{sat}$ . Notice that while

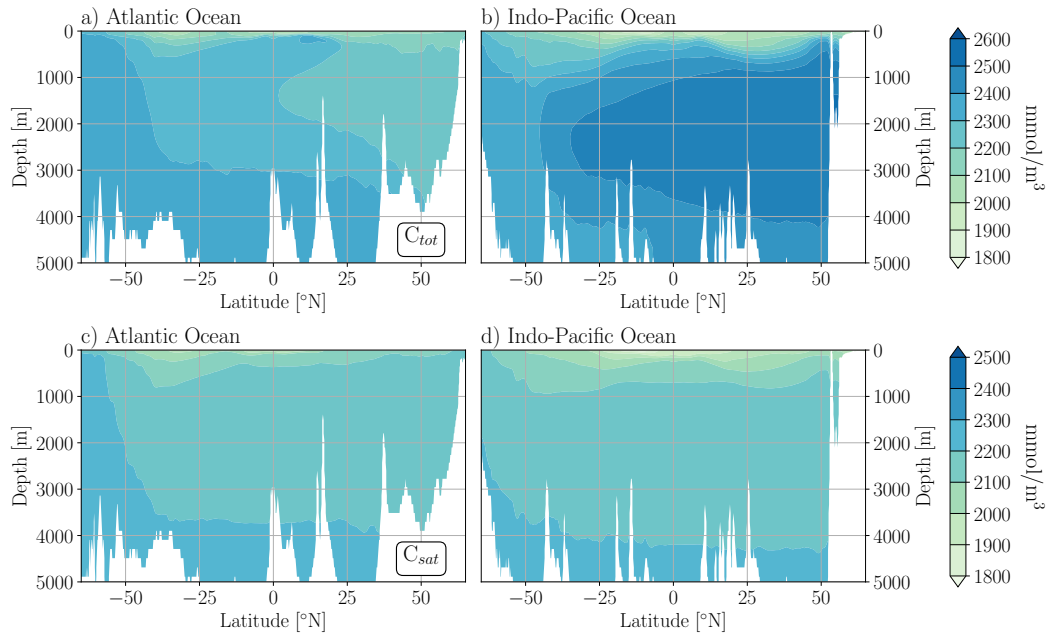


**Figure 1.** Climatological cross sections for  $C_{tot}$  (upper row) and for  $C_{sat}$  (lower row) computed from the model output of the selected ten year time period (2000-2009). Panels a and c show the Atlantic Ocean ( $25^{\circ}\text{W}$ ), and b and d show the Indo-Pacific Ocean ( $170^{\circ}\text{W}$ ).

223      $C_{sat}$  increases monotonically with depth, we can find local maxima of  $C_{tot}$  in the interior ocean. This makes  $C_{sat}$  an ideal tracer for interpretation of streamfunctions as it  
224     allows us to allocate values of  $\Psi$  to a given depth.  
225

### 226     3 Results and Discussion

227     In the following sections, we present first the latitude-depth streamfunction to help  
228     the reader with the following discussions of the latitude-carbon streamfunction (Section  
229     3.1). Next, we introduce and discuss the results of the carbon-latitude streamfunction  
230     (Section 3.2). The role of different water masses and the geographical identification of  
231     the cells are further discussed in Section 3.3. We first examine the  $C_{tot}$ -latitude stream-  
232     function for the Atlantic and Indo-Pacific oceans to better understand the underlying  
233     mechanisms of their cells and related role in the ocean carbon cycle. This simplifies the  
234     identification of different water masses. Thereafter, we separate the associated carbon  
235     transports to each of the cells to quantify their contribution to the total carbon trans-

236 port (Section 3.4). Finally, the roles of the physical and biological pumps in the merid-  
 237 ional carbon transport are discussed (Section 3.5).

### 238 3.1 The meridional overturning streamfunction

239 The meridional overturning streamfunction shows the different circulation patterns  
 240 in the Atlantic Ocean (Figure 2a) and in the Indo-Pacific (Figure 2b). The Southern Ocean  
 241 has not been split to avoid anomalous results of the streamfunction in the ACC region.

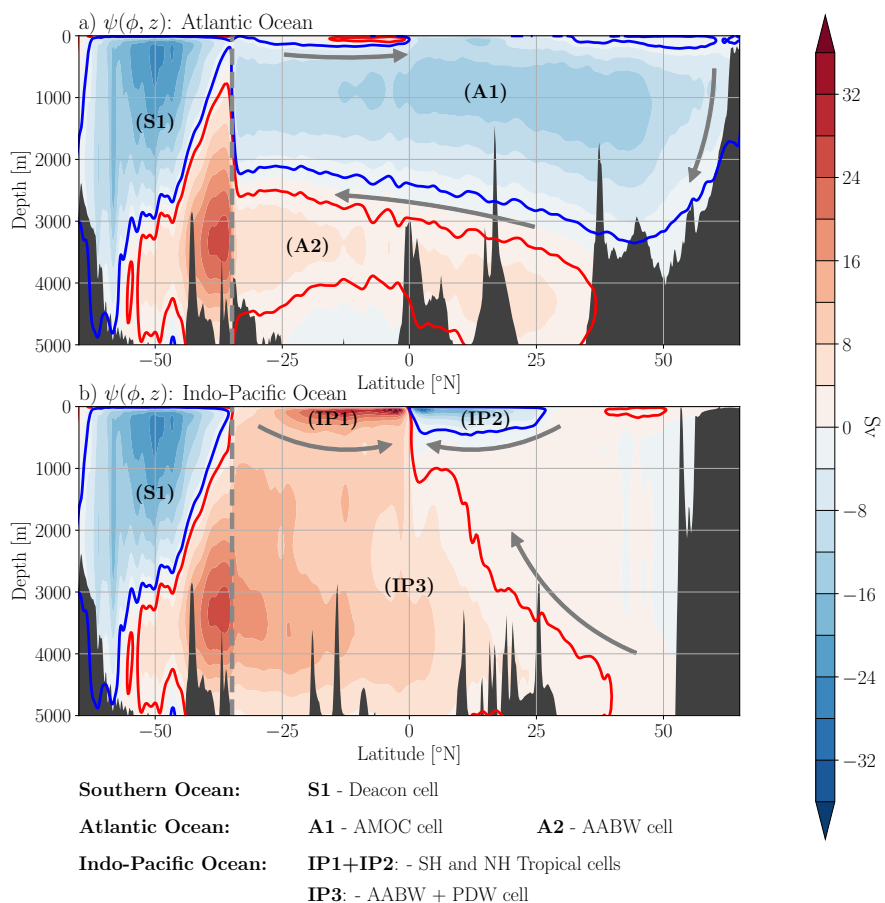


**Figure 2.** The meridional overturning streamfunction in latitude-depth space for the Atlantic Ocean (top) and the Indo-Pacific Ocean (bottom). The red (blue) cells describes counterclockwise (clockwise) circulations. The circulation of the overturning cells is given by the gray arrows. The gray dash line represents the cape Agulhas latitude.

The Atlantic Ocean is characterised by two main cells: a clockwise overturning cell (A1) located above 3000 m and spanning along all the latitudes in the basin, and an anticlockwise overturning cell (A2) located at the bottom of the basin. The former describes the northward transport of warm surface waters, their sinking at high latitudes as a result of a buoyancy loss, and the southward return flow at deeper levels. This cell is linked to the Atlantic Meridional Overturning Circulation (AMOC). The latter can be linked to the Antarctic Bottom Water (AABW) which is formed around Antarctica and is the most common water mass found at the bottom of the ocean (Talley, 2013).

The Indo-Pacific ocean is characterised by three main cells: two almost symmetric cells near the surface (IP1 and IP2), and a third cell that covers the almost the entire basin (IP3). The shallow but strong cells are a result of the wind driven circulation in the tropics. The spinning of these overturning cells describes a divergence at the surface due to the Ekman transport and a convergence of waters at the equator in deeper levels ( $\approx 500$  m) which leads to an upwelling in the region. Cell IP3 captures the Pacific Deep Water (PDW) and the AABW in the region. This cell describes a northward volume transport at the bottom and a southward volume transport at intermediate depths. Note that the strongest values are located in the Southern Hemisphere. The value of  $\Psi(\phi, z)$  in the North Pacific is very low due to the slow circulation in the region (Talley, 2013).

Finally, the Southern Ocean is characterised by a strong and deep overturning cell (S1). This cell is known as the Deacon cell and captures most of the southward Ekman return flow in the Southern Ocean. As shown by Döös and Webb (1994) this is an artefact of projecting the volume fluxes in the latitude-depth space. The Deacon cells disappears if the meridional volume fluxes are projected into the latitude-neutral density space instead.

Many of the cells that appear in  $\Psi(\phi, z)$  will have an analogous overturning cell in the latitude-carbon streamfunctions that we introduce in the coming sections.

### 3.2 The latitude-carbon streamfunction

The calculated global carbon-latitude streamfunction and its different circulation cells are shown in Figure 3a. High  $C_{tot}$  concentrations are associated with polar waters (due to higher gas solubility in colder water, e.g. Raven and Falkowski (1999); Volk and Hoffert (2013); Weiss (1974)) and deep waters (due to the biological pump, e.g. W. S. Broecker

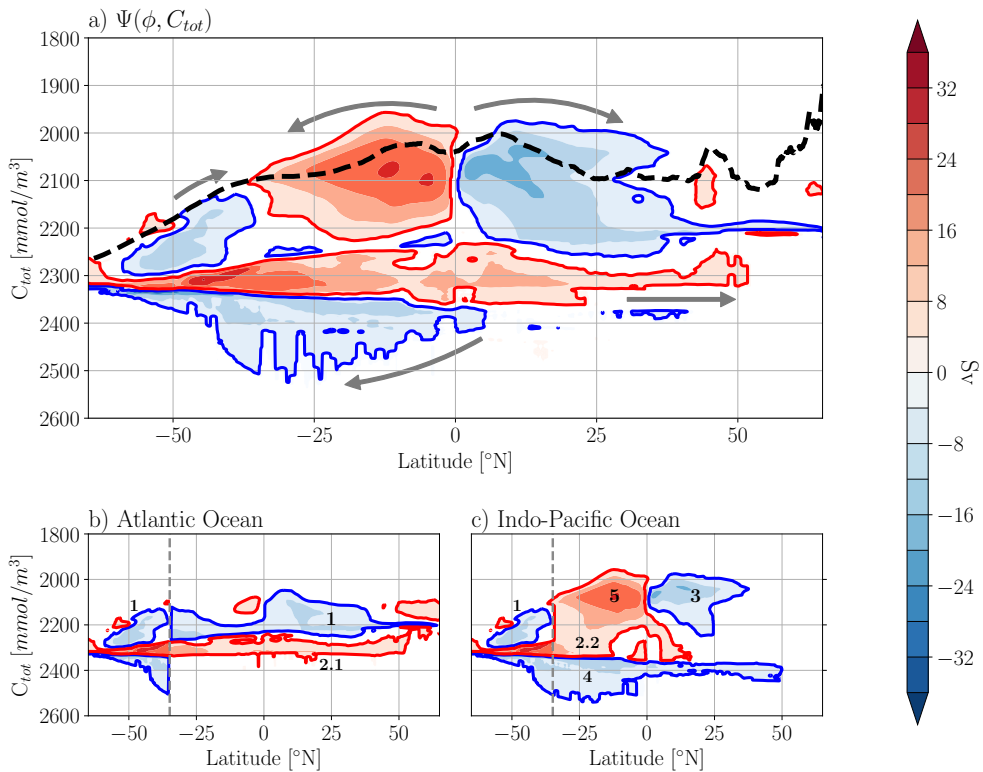


**Figure 3.** Upper panel: the global  $C_{tot}$ -latitude streamfunction. Note that the  $C_{tot}$  axes has been reversed. The red (blue) cells describe counterclockwise (clockwise) circulations. The volume weighted zonal mean surface concentration of  $C_{tot}$  is shown by the dashed black line. The lower panels represent the split of the global streamfunction into the Atlantic basin (which includes the Arctic Ocean) and the Indo-Pacific Ocean. The numbers represent the main cells of the streamfunction. The gray dashed line represents the cape Agulhas latitude.

(1983); Volk and Hoffert (2013)). For visualisation purposes, and in order to have near surface circulation cells above those associated with deep waters, the y-axis has been reversed . Note that in the Indo-Pacific the highest concentrations are located at about 2000m depth, making the interpretation of the streamfunction in this region a bit harder, which will be discussed in the next section. To illustrate the location of surface waters in relation to the circulation cells we have plotted the volume weighted zonal mean surface  $C_{tot}$  concentration (dashed black line).

The global streamfunction is characterised by five main circulation cells. The largest two surface cells are located between the equator and 40 °N/S at relatively low  $C_{tot}$  concentrations (2000–2200 mmol m<sup>-3</sup>), and are strongly linked to the big wind-driven subtropical gyres, as will be shown in Section 3.3. The cells are spinning in opposite directions, with the northern cell spinning clockwise (blue cell) and the southern one anti-clockwise (red cell). These cells transport surface waters with low  $C_{tot}$  concentrations poleward, and waters with higher  $C_{tot}$  concentrations equatorward. The increase in  $C_{tot}$  concentrations in the upper limb of these cells shows that there is a continuous uptake of atmospheric CO<sub>2</sub> in surface waters on their way poleward. In addition, another near-surface cell is observed in the Southern Ocean between 40–60° S, with  $C_{tot}$  concentrations of 2100–2300 mmol m<sup>-3</sup>, and spinning clockwise. The upper limb of this cell, is losing  $C_{tot}$  on its way northward. This cell can be linked to the activity of the ACC. The other two main cells occur with higher  $C_{tot}$  concentrations (2200–2500 mmol m<sup>-3</sup>), span whole ocean basins (i.e. stretching across the equator), and represent deep and bottom waters.

### 3.3 The role of the cells

The global streamfunction  $\Psi(\phi, \xi)$  is a composite of different cells which represent different processes and water masses. We therefore analyse the streamfunction for the two main ocean basins: the Atlantic and the Indo-Pacific Ocean, separately. In this study, we define a cell as being enclosed by the 4 Sv streamline. The identification of the main cells in the geographical (latitude-depth) space are shown in Figure 4a-b. The contours in these figures represent the fraction of volume at a given latitude and depth contained in the selected cell. The contours have been filled using a gradient colour-map where darker colours represent higher fractions.

The Atlantic basin is characterised by two main cells spanning over the entire basin (Figure 3b). The first one (referred to as cell 1) is bounded between  $C_{tot}$  concentrations between 2000 and 2250 mmol m<sup>-3</sup>, spinning clockwise, and therefore transports surface waters with low  $C_{tot}$  concentration northward, and waters with higher  $C_{tot}$  concentration southward. The re-projection of this cell in to geographical space (blue shading, in Figure 4a) shows that the majority of the cell is located at depths shallower than 1000 m, except in the mid-latitudes in the northern hemisphere where these waters can be located at almost 3000 m. This cell and its transports can be associated with the AMOC,

including the upper limb of the North Atlantic Deep Water (NADW), the tropical cell of the Northern hemisphere, and the Agulhas leakage (Talley, 2013). The NADW extends as a narrow blue feature stretching from  $\sim 40^{\circ}\text{N}$  to  $>60^{\circ}\text{S}$  at a  $C_{\text{tot}}$  concentration of  $2200 \text{ mmol m}^{-3}$  (see Figs. 1 and 3b). At  $>60^{\circ}\text{S}$ , associated with the wind-driven upwelling, or the divergence zone, in the Southern Ocean (Marshall & Speer, 2012), the lower limb of this cell reaches surface waters and then continues northward with the Ekman transport. Note that the southern tropical cell is represented by the small and weak anticlockwise cell between  $20^{\circ}\text{S}$  and the equator, however its contribution is very small. The second major cell (cell 2.1), circulating anticlockwise, spreads at narrower  $C_{\text{tot}}$  concentrations confined around  $2300 \text{ mmol/m}^3$ . It transports waters with higher  $C_{\text{tot}}$  concentration northward, and lower  $C_{\text{tot}}$  concentrations southward. The re-projection into the geographical space (orange shading in Figure 4) shows that the water masses described by this cell are located at intermediate and deeper levels, and therefore can be associated with intermediate waters, Antarctic Bottom Water (AABW) and the lower limb of North Atlantic Deep Water that upwells in the Southern Ocean (Talley, 2013).

In the Indo-Pacific Ocean three distinct cells are observed. Near the surface we find two cells of similar strength and shape, and opposite sign (cell 3 and 5). These cells span from the equator up to the mid-latitudes and cover concentrations between 2000 and  $2200 \text{ mmol m}^{-3}$ , and contain the stronger circulation in this framework, up to 30 Sv. The water masses contained in these two cells are located above 1000 m depth (green and blue shading) and represent the wind driven gyre circulation at the tropical Indo-Pacific Ocean. Similar to what we observed in the Atlantic Ocean, cell 2.2 represents the intrusion of intermediate waters from the Southern Ocean into the Indo-Pacific basin. However, in contrast to the 2.1 cell in the Atlantic, this cell does not capture the bottom waters, which in the Indo-Pacific instead are captured by cell 4. Cell 4 is spinning clockwise (see Figure 3) and is located at the highest  $C_{\text{tot}}$  concentrations observed (above  $2300 \text{ mmol m}^{-3}$ ). The water masses contained in this cell (shaded in red) can be found at any depths larger than 1000 m in the Indo-Pacific Ocean, containing the northward flowing AABW and southward flowing PDW (Talley, 2013). The clockwise circulation of this cell means that there is a net southward transport of  $C_{\text{tot}}$ , and consequently that the  $C_{\text{tot}}$  transport is larger in the PDW than in the AABW. This comes as a result of the higher  $C_{\text{tot}}$  concentrations at mid-depth in the Pacific (Figure 1).

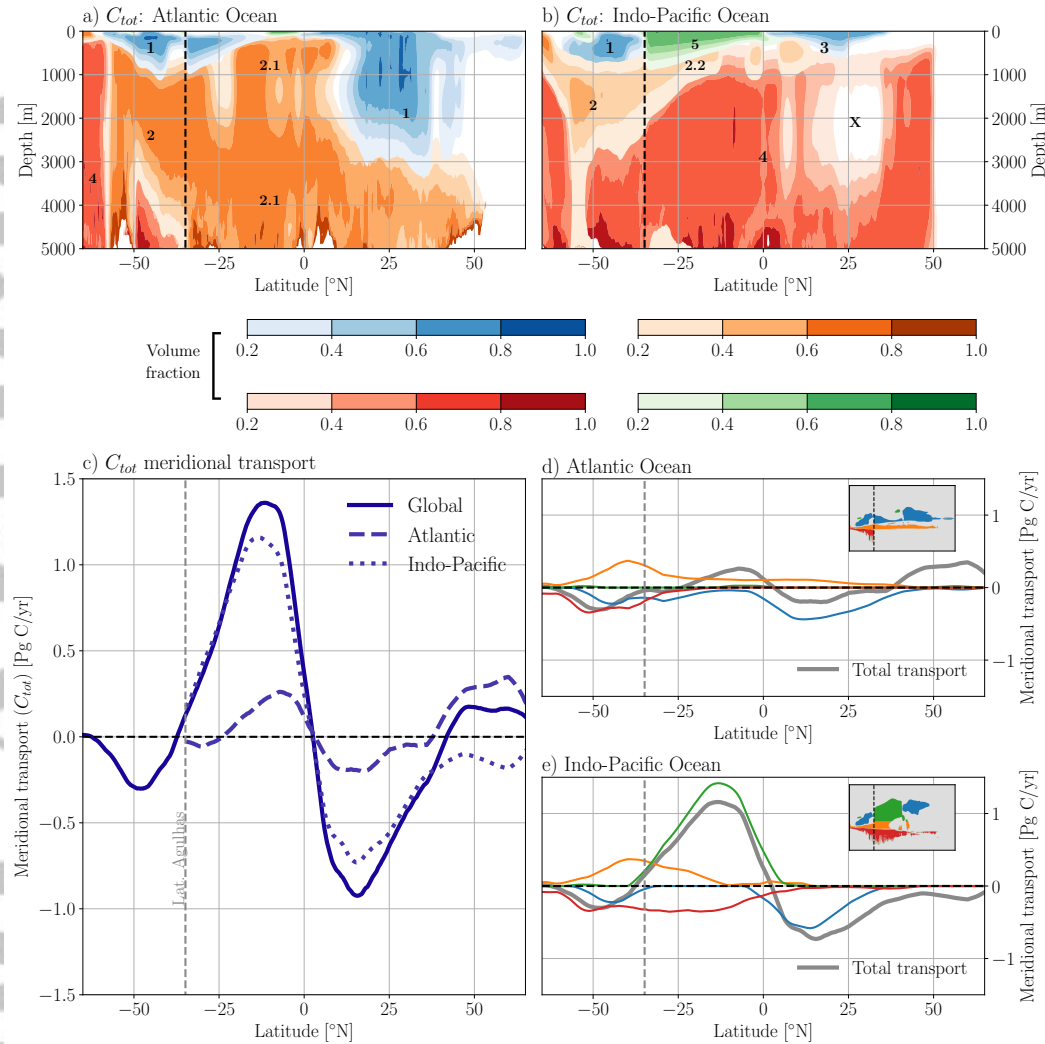


**Figure 4.** The identification of different cells (identified by numbers 1-5) for  $\Psi(\phi, C_{tot})$  in geographical space for the Atlantic (a) and the Indo-Pacific (b) basins. The contours represent the fraction of volume at a given latitude and depth contained in the selected cell. Darker colours indicate higher fractions. (c) The global meridional transport of  $C_{tot}$  and the contribution of the different basins. The contribution of each of the cells in  $\Psi(\phi, C_{tot})$  to the meridional transport for the Atlantic (d) and the Indo-Pacific basin (e). Each of the cells has an assigned colour which is used for both the transport and the re-projection plots. The transports for the cells have been computed using a threshold of 4 Sv.

344

The empty area (marked with an X) between  $20^{\circ}\text{N}$  and  $40^{\circ}\text{N}$ , and a mean depth of 2000 m can relate to a region of slow or even stagnant waters that contribute with small volume transports below our selected threshold of 4 Sv. This is coined the shadow

345

346

347 zone (de Lavergne et al., 2017). The sluggishness of these waters becomes apparent when  
 348 observing that they coincide with the oxygen minimum and the  $C_{tot}$  maximum zone in  
 349 the North Pacific Ocean (Figure S1 in supplementary material). Note that the  $C_{tot}$  max-  
 350 imum zone is not located at the bottom of the basin (as it is the case for the Atlantic  
 351 and the Southern Ocean), confounding the use of  $C_{tot}$  as a pseudo-depth.

### 352 3.4 Associated carbon transports

353 The global transport of  $C_{tot}$  (Figure 4c) is described by a convergence of carbon  
 354 at the equator and a divergence region at around 30°S. The maximum carbon transports  
 355 are observed in the tropics around 20°N/S with a maximum northward  $C_{tot}$  transport  
 356 of 1.4 Pg C yr<sup>-1</sup> in the southern hemisphere and a maximum southward transport of  
 357 0.9 Pg C yr<sup>-1</sup> in the northern hemisphere (Figure 4c). The carbon transport convergence  
 358 is a result of the strong surface tropical cells that transport carbon equatorward where  
 359 it is outgassed to the atmosphere because of the low solubility in the warm tropical wa-  
 360 ter. The divergence of  $C_{tot}$  at about 30°S in the Southern Ocean is mainly caused by  
 361 the net southward transport of cell 1, and the net northward transport of cell 5. It is as-  
 362 sociated with the Southern Ocean subduction zone, where northward flowing surface wa-  
 363 ters of the Southern Ocean is subducted below warmer subtropical waters (Speer et al.,  
 364 2000).

**Table 1.** Maximum carbon transport for each of the cells in Pg C yr<sup>-1</sup>

Cell	basin	$C_{tot}$ (mean)	$C_{tot}$ (max)	$C_{sat}$ (mean)	$C_{sat}$ (max)	Primary Association
1	Atlantic	-0.13	-0.44	-0.19	-0.56	AMOC
2.1	Atlantic	0.10	0.37	0.08	0.27	Intermediate waters/AABW
2.2	Indo-Pacific	0.12	0.37	0.12	0.27	Intermediate waters
3	Indo-Pacific	-0.25	-0.58	-0.22	-0.47	ST Gyre
4	Indo-Pacific	-0.14	-0.35	—	—	Deep/Bottom Water
5	Indo-Pacific	0.44	1.42	0.36	1.14	ST Gyre

365 The global signal is mainly dominated by the transports in the Indo-Pacific Ocean.  
 366 Different factors are responsible for this: the width of the basin, the higher concentra-  
 367 tions of  $C_{tot}$  in the Indo-Pacific and the role of the surface tropical cells. The cells con-

tribute in different ways to the  $C_{tot}$  transport as they represent different dynamical and/or biogeochemical processes (See Figure 4e). Both cell 5 (green) and cell 3 (blue) are the largest contributors to the meridional transport in the Indo-Pacific Ocean, and also on a global scale, with  $C_{tot}$  transports amounting to  $1.42 \text{ Pg C yr}^{-1}$  and  $-0.58 \text{ Pg C yr}^{-1}$ , respectively. The larger absolute transport in cell 5 compared to cell 3 can, to a large extent, be explained by the wider southern part of the Indo-Pacific. As mentioned in the previous section, these tropical cells represent the near surface wind driven tropical circulation. A combination of the strong dynamical cells and the upwelling of carbon rich waters from deeper waters results in a strong equatorward transport in the tropics. The tropical cells are described in temperature-salinity coordinates by Döös et al. (2012); Zika et al. (2012); Groeskamp et al. (2014) and in latitude-density coordinates by Ballarotta et al. (2014). Cell 4, which consist of AABW and PDW, has a net southward transport of carbon, amounting to  $-0.35 \text{ Pg C yr}^{-1}$ . This substantial carbon transport is a result of the high concentrations of  $C_{tot}$  which compensates the small volume fluxes in the deeper layers.

The Atlantic basin contributes with much weaker transports (Figure 4d). The Atlantic meridional transport of carbon is the result of a compensation between the southward  $C_{tot}$  transport driven by cell 1 (amounting to  $-0.44 \text{ Pg C yr}^{-1}$ ) and the northward transport driven by  $C_{tot}$  rich waters in the AABW in cell 2.1 (up to  $0.37 \text{ Pg C yr}^{-1}$ ). It is important to note that cell 1 not only includes the NADW, but also includes the tropical cell of the North Atlantic. There is a small convergence at the equatorial regions driven by the weak tropical cells in the basin.

### 3.5 The role of the physical and biological pumps

The dominant component in the solubility pump (see Section 2.1) is saturation carbon,  $C_{sat}$ . Therefore, the associated streamfunction  $\Psi(\phi, C_{sat})$  (Figure 5) gives a good first approximation of the role of the solubility pump in the ocean carbon transport. There is a striking similarity with the density-latitude streamfunction (shown in e.g. Ballarotta et al. (2014)), which can be explained by the strong control that temperature exerts on  $C_{sat}$  (Weiss, 1974) and density.

It is not surprising to find many similarities between  $\Psi(\phi, C_{sat})$  and  $\Psi(\phi, C_{tot})$ , as  $C_{sat}$  is the largest contributor to the total carbon in the ocean (Williams & Follows, 2011). The global streamfunction is characterised by three main cells. Similar to  $\Psi(\phi, C_{tot})$  we

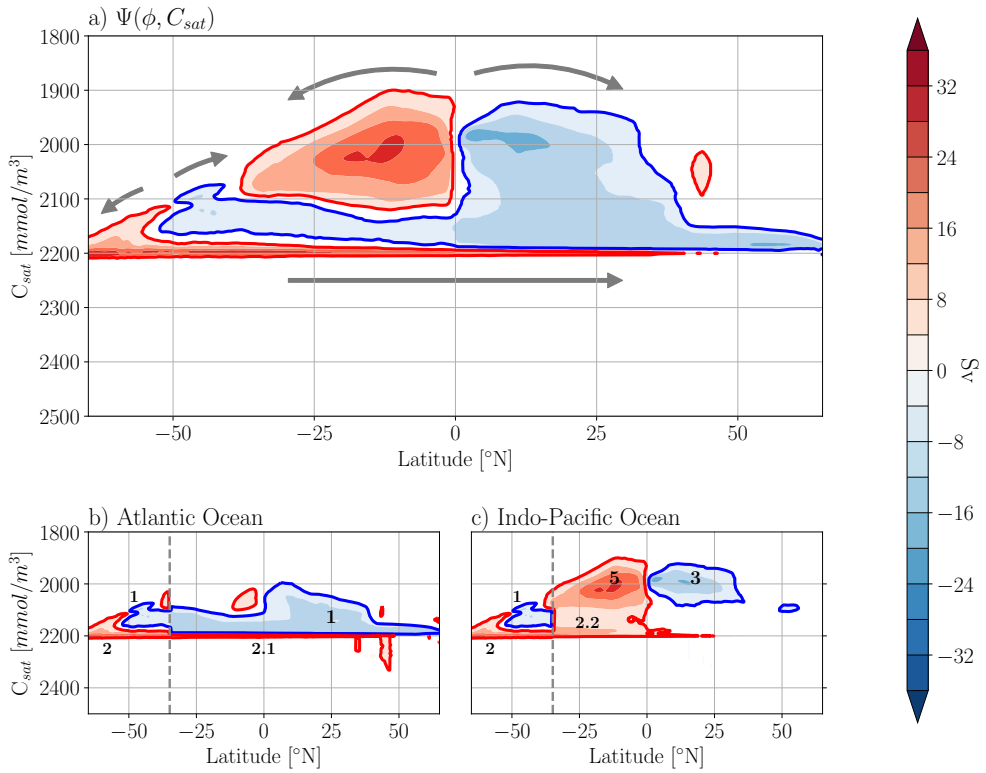


**Figure 5.** Upper panel: the global  $C_{sat}$ -latitude streamfunction. The lower panels represent the split of the global streamfunction into the Atlantic basin (which includes the Arctic Ocean) and the Indo-Pacific Ocean. The gray dashed line represents the cape Agulhas latitude. The  $C_{sat}$  axes has been reversed so that the tracer acts as a pseudo-depth, where the low values are found near the surface and the higher values at deeper depths. The red (blue) cells represent counterclockwise (clockwise) circulations.

400 can distinguish the two surface tropical cells and the surface cell in the Southern Ocean;  
 401 however, the Southern ocean cell is directly connected to the northern tropical cell. An  
 402 analogue to the deep antitropical cell can be found in  $\Psi(\phi, C_{sat})$  confined to a much  
 403 narrower  $C_{sat}$  concentration around 2200 mmol m<sup>-3</sup>. Interestingly, the deep clockwise  
 404 cell found in  $\Psi(\phi, C_{tot})$  is not found in  $\Psi(\phi, C_{sat})$ . This will be discussed further below.

405 The different circulation patterns of the Atlantic and the Indo-Pacific basin are cap-  
 406 tured by  $\Psi(\phi, C_{sat})$ . By splitting the streamfunction into separate basins, we facilitate  
 407 the identification of the different circulation patterns, and their role in the oceanic car-

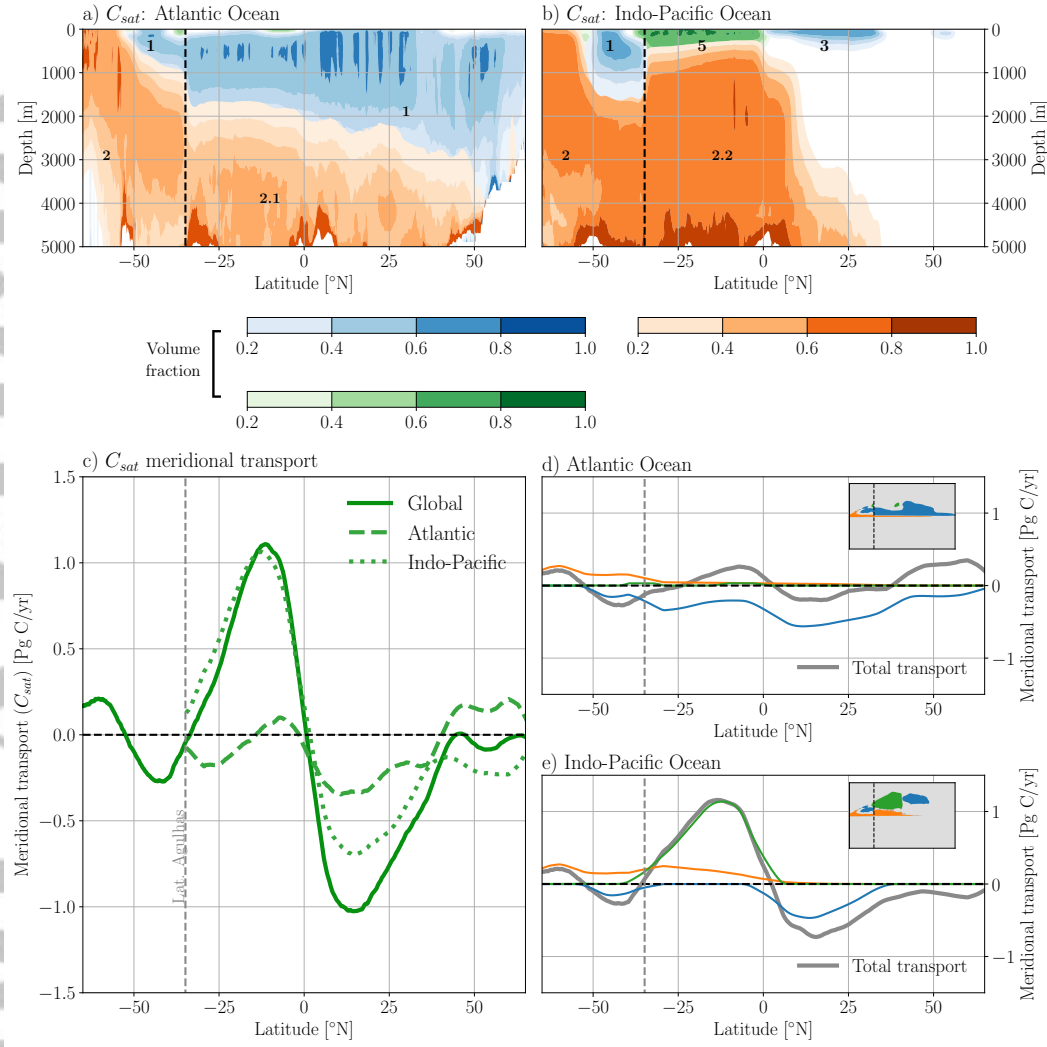


**Figure 6.** The identification of different cells for  $\Psi(\phi, C_{sat})$  in geographical space for the Atlantic (a) and the Indo-Pacific (b) basins. The contours represent the fraction of volume at a given latitude and depth contained in the selected cell. Darker colours indicate higher fractions. (c) The global meridional transport of  $C_{sat}$  and the contribution of the different basins. The contribution of each of the cells in  $\Psi(\phi, C_{sat})$  to the meridional transport for the Atlantic (d) and the Indo-Pacific basin (e). Each of the cells has an assigned colour which is used for both the transport and the re-projection plots. The transports for the cells have been computed using a threshold of 4 Sv.

408

bon cycle, compared to the global streamfunction (see Figure 5). The cells in the Atlantic ocean play the same role as in  $\Psi(\phi, C_{tot})$ , where cell 1 represents the AMOC and cell 2.1 the bottom waters (Figure 5b). In the Indo-Pacific, the tropical cells (cells 5 and

409

410

411 3), and the Intermediate waters (cell 2.2) are captured by  $\Psi(\phi, C_{sat})$ . The re-projection  
 412 of the cells into geographical space (Figure 6a-b) confirms that the cells in  $\Psi(\phi, C_{sat})$   
 413 are a projection in the carbon space of the meridional overturning circulations in both  
 414 basins (see Figure 2).

415 The global transport of  $C_{sat}$  is dominated by the Indo-Pacific basin, especially in  
 416 the Southern Hemisphere, with a maximum equatorward transport of  $1.1 \text{ Pg C yr}^{-1}$  (Figure  
 417 6). The surface tropical cells control most of the meridional transport in the Indo-  
 418 Pacific ocean. In the Atlantic, the cell linked to the AMOC carries carbon southward  
 419 with a maximum value of  $0.56 \text{ Pg C yr}^{-1}$  at  $18^\circ\text{N}$ . This cell transports a larger amount  
 420 of  $C_{sat}$  than  $C_{tot}$ . This is a consequence of the under-saturation of the waters that de-  
 421 scend in the North Atlantic to form NADW (Eggleston & Galbraith, 2018), which re-  
 422 sults in a transport of  $C_{dis}$ .

423 The most striking difference in the Indo-Pacific streamfunction for  $C_{sat}$  compared  
 424 to  $C_{tot}$  is that it does not capture cell 4. This suggests that the solubility pump is not  
 425 responsible for the transport that occurs in this cell. The residual between the transport  
 426 of  $C_{tot}$  and  $C_{sat}$  ( $C_{bio+res}$ , see Equation 2) represents transport of the inorganic carbon  
 427 in the ocean resulting from mainly biochemical processes. There is also a contribution  
 428 from the disequilibrium term and the anthropogenic carbon.  $C_{bio+res}$  is not a conser-  
 429 vative tracer as  $C_{bio}$  has internal sources and sinks. Therefore, the associated stream-  
 430 function  $\Psi(\phi, C_{bio+res})$  is less straightforward to interpret.

431 Biological and disequilibrium processes are highly important for air-sea gas exchange  
 432 (Sarmiento & Gruber, 2006). However, when studying Figures 4, 6 and Table 1, it be-  
 433 comes clear that  $C_{bio+res}$  contributes to a relatively small part of the total carbon trans-  
 434 port in all cells. The only exception is cell 4, which solely transports  $C_{bio+res}$ . From Fig-  
 435 ure S11 in the supplementary material, we see that the  $C_{bio+res}$  in this deep cell comes  
 436 mostly from the biological pump, and contains little anthropogenic or disequilibrium car-  
 437 bon. This suggests that the biological pump allows for carbon storage in the shadow zone  
 438 (Section 3.3), while the solubility pump is inefficient.

### 439 3.6 Carbon budget and eddy-driven transport

440 The aim of this section is to present a budget (Figure 7) showing the carbon trans-  
 441 port between different regions of the global ocean together with the local air-sea  $\text{CO}_2$

exchange and accumulation, and to give an estimate of the eddy-driven transport. Due to mass conservation, the transport of inorganic carbon by the ocean circulation has to match boundary fluxes, accumulation, eddy-driven transport, and transport of organic carbon. The eddy-driven transport is not captured in our data because of the coarse time-resolution, but it can be computed knowing all other fluxes. Because of the constant forcing of anthropogenic carbon, the ocean carbon system is not in steady state, and there is a net accumulation of  $1.73 \text{ Pg C yr}^{-1}$  of anthropogenic carbon. Boundary fluxes include air-sea  $\text{CO}_2$  exchange and sediment-water C exchange. The net sediment  $\text{CO}_2$  fluxes, as well as the meridional transport of organic carbon, in our model are negligible, and we therefore leave them out.

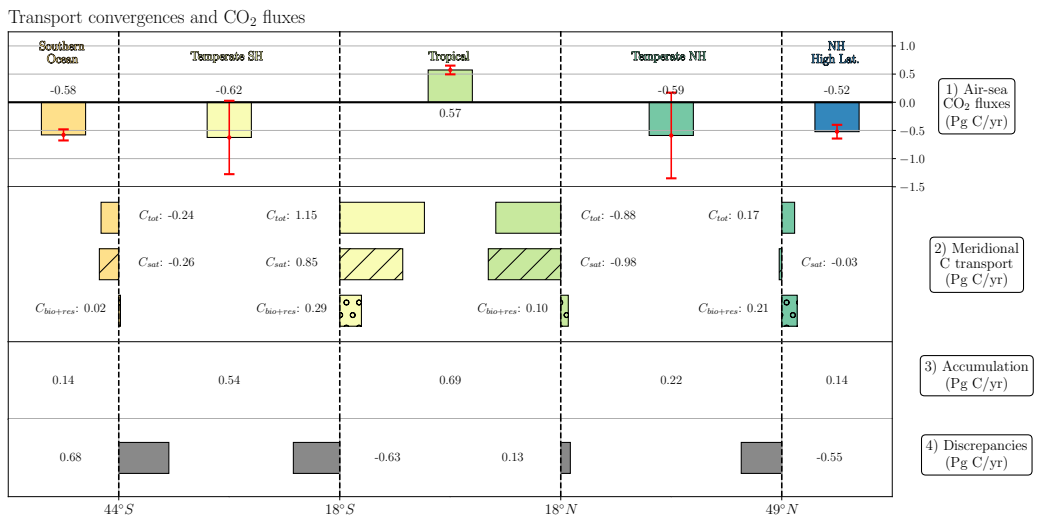


**Figure 7.** Carbon budget in the ocean for different regions. Upper panel: integrated  $\text{CO}_2$  surface fluxes for different regions, the red error bars represent the standard deviation of the fluxes. The meridional transports of  $C_{tot}$  at given latitudes and the contribution of the different components are represented in the second panel. The accumulation of carbon as a result of the anthropogenic carbon are shown in the third panel. The last row represents the discrepancy terms required to close the budget. Units are given in  $\text{Pg C yr}^{-1}$ .

The top part of Figure 7 shows the net air-sea  $\text{CO}_2$  fluxes. There is a net uptake of carbon in all the regions except in the tropical one where there is a net outgassing. The red bars represent the standard deviation of those fluxes showing high variability in the temperate regions in both hemispheres. This large variability is a result of the sea-

sonal changes in temperature and primary production that impact the ocean carbon uptake. The net uptake of carbon in this study is  $1.73 \text{ Pg C yr}^{-1}$ . The flux distribution and the net uptake value are in good correspondence with values found in literature (Mikaloff Fletcher et al., 2007; Gruber et al., 2009).

The next set of bars represents the meridional carbon transport of  $C_{tot}$ ,  $C_{sat}$  and  $C_{bio+res}$  at given latitudes.  $C_{bio+res}$  includes all terms not represented by  $C_{sat}$ . As described in Section 3.5, the transport of  $C_{sat}$  is the major contributor to the total meridional transport of carbon. However, in the high-latitude Northern Hemisphere,  $C_{bio+res}$  is dominant in the total transport. Below the transport bars, the accumulation of carbon in each region is shown. The tropics are the region with the largest accumulation rate ( $0.69 \text{ Pg C yr}^{-1}$ ) followed by the south-hemispheric temperate region ( $0.54 \text{ Pg C yr}^{-1}$ ). The northern hemisphere, especially at high latitudes, showed the lowest accumulation rates.

The accumulation in each of the regions and the convergence/divergence of carbon transports are not enough to close the carbon budget. Therefore, the discrepancy terms are shown in the last panel. These discrepancies are computed by closing the carbon budget at each of the latitudinal regions starting from the Southern Ocean. The dominant contributors to these discrepancies are likely to be the effect of diffusivity and the frequency of the output data. As our data are output with a monthly frequency, we do not capture the carbon transports advected by eddies at smaller time scales.

#### 4 Turnover time

More information on the role of the circulation cells in keeping  $\text{CO}_2$  from the atmosphere is obtained when looking at their turnover times. The turnover time,  $\tau$  gives an estimate of how much time is required for the entire volume contained between two streamlines to complete a cycle in the cell. That is:

$$\tau = \frac{\Delta V}{\Delta \Psi} \quad (7)$$

where  $\Delta \Psi$  represents the selected streamlines and  $\Delta V$  is the volume contained in between those streamlines. The turnover times for  $\Psi(\phi, C_{tot})$  are presented in Figure 8, we have selected intervals of 4 Sv between streamlines.

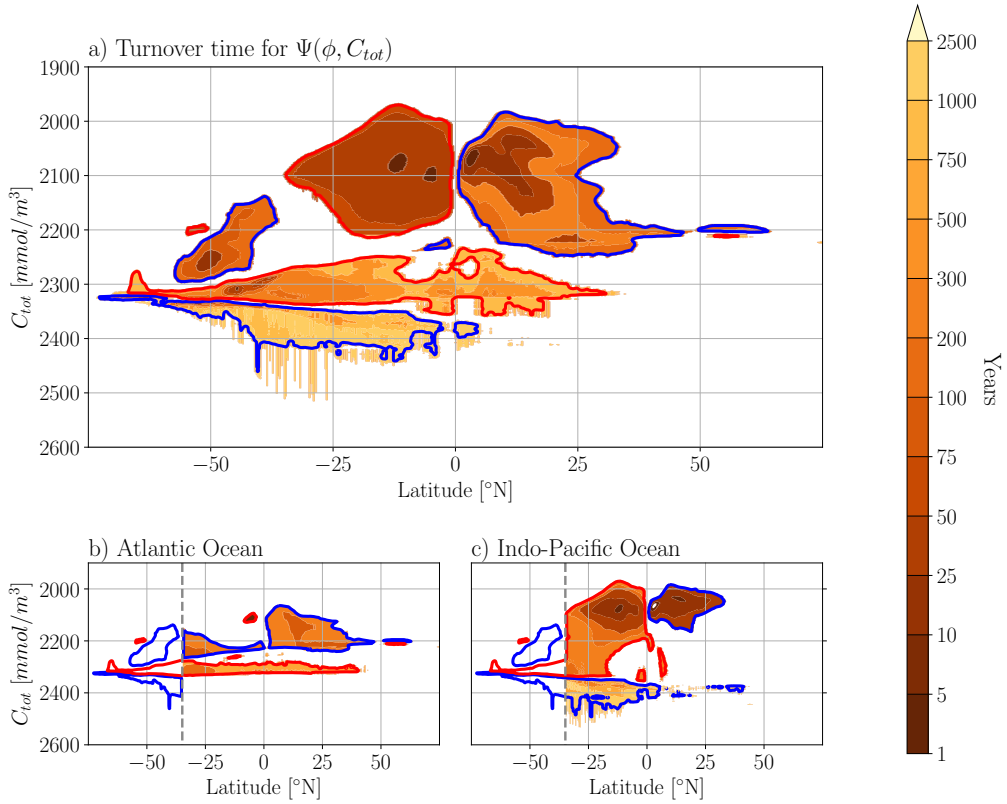


**Figure 8.** The turnover times computed from  $\Psi(\phi, C_{tot})$  for the global case (a) and for the two basins: Atlantic (b) and Indo-Pacific (c). The streamline interval has been chosen to 4 Sv. Units given in years.

The near-surface cells have short turnover times of the order of decades, this result is not surprising as these cells are both the strongest and are confined in a small volume. The decomposition of the streamfunction shows that the tropical cells in the Indo-Pacific Ocean are those with the shortest turnover times (<50 years), followed by the AMOC cell (around 100-300 years) and the bottom cell in the Atlantic (300-500 years). The longest time scales, on the order of more than 1000 years, are associated with the deep cell in the Indo-Pacific Ocean. As this cell only consists of  $C_{bio}$ , it indicates that the biological pump in the Indo-Pacific is the most important process for storing  $\text{CO}_2$  from the atmosphere on longer time scales.

**493 5 Conclusions**

494 As the largest dynamic reservoir of carbon in the Earth system, the ocean plays  
495 an important role in influencing climate. However, understanding its carbon cycle is com-  
496 plicated by of the diverse roles played by its water masses, circulation and biogeochem-  
497 ical processes, and separating these processes in observational data or model output us-  
498 ing traditional methods is difficult. In this study we show how to apply latitude-tracer  
499 streamfunctions, a diagnostic tool well-known in physical oceanography to facilitate the  
500 understanding of processes in the ocean. We have chosen to focus on the ocean's dissolved  
501 inorganic carbon pool as this buffers the atmospheric concentration of CO<sub>2</sub> that has an  
502 important role in climate.

503 This diagnostic tool connects a commonly-used framework for understanding of the  
504 ocean circulation (streamfunctions) with a commonly-used framework for understand-  
505 ing the ocean carbon cycle and its sources and sinks (carbon separation). This way, we  
506 are able to separate the roles played by different water masses and circulation pathways  
507 on the carbon cycle. We find that the shallow subtropical gyres are the main contrib-  
508 utor to meridional carbon transport in the ocean, carrying carbon from the mid-latitudes  
509 into the equatorial region. According to our model, they transport up to 1.42 Pg C yr<sup>-1</sup>,  
510 while the overturning represented by deeper water masses such as the AABW and PDW  
511 only carry up to 0.35 Pg C yr<sup>-1</sup>. By separating the carbon into its different constituents,  
512 we are additionally able to show that the carbon transported in the subtropical cells and  
513 the deep Atlantic mainly originates from the the solubility pump and thus air-sea ex-  
514 change of CO<sub>2</sub>, while the carbon transport in the deep Pacific is mainly of biogenic ori-  
515 gin.

516 For the studies of future climate variability and CO<sub>2</sub> uptake by the ocean, this method  
517 can simplify model intercomparisons, and allow us to put error bars on the role of dif-  
518 ferent water masses in future ocean carbon uptake/release. It will allow us to identify  
519 notable changes in ocean carbon transport and identify the responsible processes. A fur-  
520 ther advantage of this streamfunction methodology is the possibility of computing the  
521 turnover time of each of the cells. Insights gained from studying turnover time can be  
522 helpful in understanding changes in ocean carbon transport across climate states (e.g.  
523 glacial-interglacial cycles). In this way, this tool can advance, and provide more detail  
524 to, the understanding of the oceans role in carbon sequestration.

## 525 Appendix A Discretisation of the streamfunction

526 We will here explain how we computed  $\Psi(\phi, \xi)$  by numerical discretisation of equa-  
 527 tion (4), using finite differences. Let us consider a gridded 3D field for the total merid-  
 528 ional velocity  $v_{i,j,k,n}$  and the tracer field  $\xi_{i,j,k,n}$ , where  $i, j, k$  represent the spatial indexes  
 529 and  $n$  represents the time index. Moreover, we will define a discretised space of the tracer  
 530  $\xi_m^D$  as a function of the index  $m$ , so that  $\xi_m^D = \xi_{min}^D + (m - 1)\Delta\xi$ .

531 The streamfunction in the discrete form can be written as,

$$\psi_{j,m} = \frac{1}{N} \sum_{n=1}^N \sum_{i=1}^I \sum_{k=1}^K v_{i,j,k,n} \mu[m - l_{i,j,k,n}] \Delta z_{i,j,k} \Delta x_{i,j} \quad (\text{A1})$$

532 where  $N$  is the total number of time steps consider,  $I$  and  $K$  are the maximum value  
 533 of the zonal and vertical indexes. Besides,  $\mu[*]$  is the discrete unit function where  $l_{i,j,k,n}$   
 534 is the index corresponding to the nearest  $\xi_l^D$  for  $\xi_{i,j,k,n}$  ( $l_{i,j,k,n} = 1 + \lfloor \frac{\xi_{i,j,k,n} - \xi_{min}^D}{\Delta\xi} + 0.5 \rfloor$ ).

## 535 Appendix B A note about discretisation

536 The meridional tracer transport can be computed directly by integrating the stream-  
 537 function in the continuous form. However, this direct relationship does not hold directly  
 538 in the discrete form. There are two main sources of error in the computation: the res-  
 539 olution of the binning space, and the choice of the minimum and maximum value of the  
 540 range.

541 The discrete version of the meridional transport computed directly from the ve-  
 542 locity and the tracer fields is given by the equation:

$$Tr_j^{(1)} = \frac{1}{N} \sum_{n=1}^N \sum_{i=1}^I \sum_{k=1}^K v_{i,j,k,n} (\xi_{i,j,k,n} - \xi_{ref}) \Delta z_{i,j,k} \Delta x_{i,j}. \quad (\text{B1})$$

543 Similarly, the discrete version of the meridional tracer transport computed from the stream-  
 544 function (equation (5)) is given by,

$$Tr_j^{(2)} = \sum_{m=1}^{M-1} (\xi_m^D - \xi_{ref}) \frac{\psi_{j,m+1} - \psi_{j,m}}{\Delta\xi} \Delta\xi = \sum_{m=1}^{M-1} (\xi_m^D - \xi_{ref}) (\psi_{j,m+1} - \psi_{j,m}). \quad (\text{B2})$$

545 Inserting the definition of the discretised streamfunction (equation(A1)) we can obtain  
 546 the following expression for the discretised transport:

$$\begin{aligned} Tr_j^{(2)} &= \frac{1}{N} \sum_{n=1}^N \sum_{i=1}^I \sum_{k=1}^K v_{i,j,k,n} \left( \sum_{m=1}^{M-1} (\xi_m^D - \xi_{ref}) \delta[m - l_{i,j,k,n}] \right) \Delta z_{i,j,k} \Delta x_{i,j} = \\ &= \frac{1}{N} \sum_{n=1}^N \sum_{i=1}^I \sum_{k=1}^K v_{i,j,k,n} (\xi_{i,j,k,n}^D - \xi_{ref}) \Delta z_{i,j,k} \Delta x_{i,j}. \end{aligned} \quad (\text{B3})$$

547 In contrast to equation (B1) the tracer field in this case is given by the nearest value in  
 548 the discrete space.

549 We will denote as the residual transport,  $\epsilon$ , the difference between the transport  
 550 computed directly and the one computed from the streamfunction:

$$\begin{aligned}\epsilon &\equiv Tr_j^{(1)} - Tr_j^{(2)} = \frac{1}{N} \sum_{n=1}^N \sum_{i=1}^I \sum_{k=1}^K v_{i,j,k,n} (\xi_{i,j,k,n} - \xi_{i,j,k,n}^D) \Delta z_{i,j,k} \Delta x_{i,j} \\ &= \frac{1}{N} \sum_{n=1}^N \sum_{i=1}^I \sum_{k=1}^K v_{i,j,k,n} \delta \xi_{i,j,k,n} \Delta z_{i,j,k} \Delta x_{i,j},\end{aligned}\quad (B4)$$

551 where  $\delta \xi_{i,j,k,n}$  represents the difference between the original and the nearest value in the  
 552 discrete space of the tracer. This term is bounded by the resolution of the tracer  $\Delta \xi$ ,

$$\epsilon = |\mathcal{O}(\delta \xi_{i,j,k,n})| \leq \mathcal{O}(\Delta \xi). \quad (B5)$$

553 A coarse resolution in the binning will have as a result a over-estimation or a sub-estimation  
 554 of the transports. This residual transport will decrease in a finer resolution.

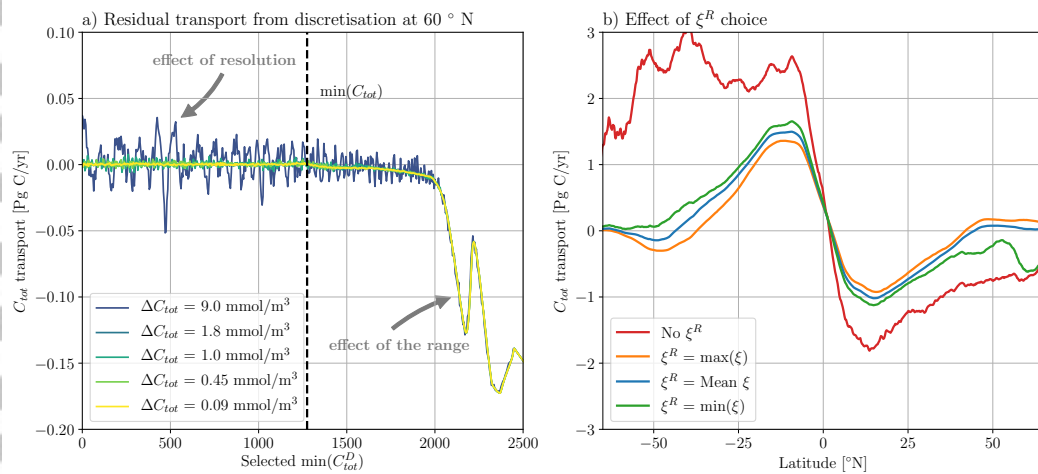


**Figure B1.** (a): The residual transport at 60°N as a result of the discretisation. The solid colour lines represent different resolutions of the discretised tracer space. If the selected range includes all the possible values of the tracer the residual transport depends only on the resolution. The minimum value of  $C_{tot}$  is represented by the dashed line. (b): The global transport for  $C_{tot}$  for different choices for  $\xi^R$ . A right choice of this value will minimise the effect of divergence. If the system would be non divergent the results for the transport would become insensitive to the choice of  $\xi^R$ .

555        The selected range for the tracer is also important. The range should include all  
 556        the possible values of the tracer. If a value of the tracer is outside the range, the trans-  
 557        port associated to that water mass will be miscalculated. This error can be reduced by  
 558        selecting a range that covers all the possible values of the tracer. In Figure B1a we rep-  
 559        resent the residual transport at 60°N for different resolutions and minimum values of the  
 560        tracer in the discrete form. In all the cases the maximum value of tracer is kept constant.  
 561        If our discrete space includes all the possible values of the tracer, the residual transport  
 562        is a result of the discretisation. The resolution used in this study ( $\Delta C_{tot} = 1.0 \text{ mmol m}^{-3}$ )  
 563        is fine enough to obtain a negligible residual transport. The effect of the selected range  
 564        has a significant impact as our domain includes fewer of the possible values of the tracer.  
 565        This residual transport is independent of the chosen resolution.

566        Another important factor is the choice of the reference tracer value,  $\xi^R$ , when com-  
 567        puting the meridional transport. The computed transports are sensitive to this choice  
 568        in regions with large volume transports (here, the Southern Ocean, see Figure B1b). By  
 569        using the mean value rather than the minimum or maximum, our computed transports  
 570        provide a plausible estimate between the two extremes.

## 571        Acknowledgments

572        This work has been financially supported by the Bolin Centre for Climate Research. F.F.  
 573        wants to acknowledge Bolin Center for Climate Research, research areas 1 (Oceans – at-  
 574        mosphere dynamics and climate) and 4 (Biogeochemical cycles and climate), for fund-  
 575        ing. SG acknowledge support from the Australian Research Council Grant FL150100090.  
 576        The modelling component of this work used the ARCHER UK National Supercomput-  
 577        ing Service (<http://www.archer.ac.uk>), and was primarily supported by NERC National  
 578        Capability funding and the Regional Ocean Modelling project (ROAM; grant NE/H017372/1).  
 579        The analysis and storage of data were performed on resources provided by the Swedish  
 580        National Infrastructure for Computing (SNIC) at the National Centre at Linköping Uni-  
 581        versity (NSC). Fortran codes used for the data analysis and computation of the stream-  
 582        functions in Section 2.2 are available from GitHub (<https://doi.org/10.5281/zenodo.3256350>). Relevant model output data, streamfunctions and the meridional transports  
 583        computed in this study are available from Zenodo (<https://doi.org/10.5281/zenodo.3254449>). This manuscript has benefited from discussions with Kevin I. C. Oliver, Gur-  
 584        van Madec, Casimir de Lavergne, and David Ferreira and the authors would like to thank  
 585  
 586

587 them for their useful comments. The authors also would like to thank the two anonymous  
 588 reviewers that substantially improved the manuscript.

## 589 References

- 590 Ballarotta, M., Falahat, S., Brodeau, L., & Döös, K. (2014). On the glacial  
 591 and interglacial thermohaline circulation and the associated transports  
 592 of heat and freshwater. *Ocean Science*, 10(6), 907–921. Retrieved from  
 593 <https://www.ocean-sci.net/10/907/2014/> doi: 10.5194/os-10-907-2014
- 594 Brewer, P. G., Goyet, C., & Dyrssen, D. (1989). Carbon dioxide transport by  
 595 ocean currents at 25°N latitude in the Atlantic Ocean. *Science*, 246(4929),  
 596 477–479. Retrieved from <http://www.sciencemag.org/cgi/doi/10.1126/science.246.4929.477>  
 597 doi: 10.1126/science.246.4929.477
- 598 Broecker, W., & Peng, T. (1992). Interhemispheric transport of carbon dioxide by  
 599 ocean circulation. *Nature*, 356, 587–589. Retrieved from <http://www.nature.com/nature/journal/v356/n6370/abs/356587a0.html>
- 600 Broecker, W. S. (1983). The ocean. *Scientific American*, 249(3), 146–161.
- 601 Caias, P., Sabine, C., Bala, G., Bopp, L., Brovkin, V., Canadell, J., ... Thorn-  
 602 ton, P. (2013). Carbon and other biogeochemical cycles [Book Section]. In  
 603 T. Stocker et al. (Eds.), *Climate change 2013: The physical science basis.  
 604 contribution of working group i to the fifth assessment report of the inter-  
 605 governmental panel on climate change* (pp. 465–570). Cambridge, United  
 606 Kingdom and New York, NY, USA: Cambridge University Press. Retrieved  
 607 from [www.climatechange2013.org](http://www.climatechange2013.org) doi: 10.1017/CBO9781107415324.015
- 608 Couldrey, M. P. (2018). *Mechanisms of ocean carbon cycle variability in the 21st  
 609 century* (Doctoral dissertation, University of Southampton). Retrieved from  
 610 <https://eprints.soton.ac.uk/421105/>
- 611 de Lavergne, C., Madec, G., Roquet, F., Holmes, R. M., & McDougall, T. J. (2017).  
 612 Abyssal ocean overturning shaped by seafloor distribution. *Nature*, 551(7679),  
 613 181–186. Retrieved from <http://dx.doi.org/10.1038/nature24472> doi: 10  
 614 .1038/nature24472
- 615 Döös, K., Nilsson, J., Nycander, J., Brodeau, L., & Ballarotta, M. (2012). The world  
 616 ocean thermohaline circulation. *Journal of Physical Oceanography*, 42(9),  
 617 1445–1460. Retrieved from <https://doi.org/10.1175/JPO-D-11-0163.1>

- 619 doi: 10.1175/JPO-D-11-0163.1
- 620 Döös, K., & Webb, D. J. (1994). *The Deacon cell and the other meridional cells of*  
621 *the Southern Ocean* (Vol. 24) (No. 2). doi: 10.1175/1520-0485(1994)024<0429:  
622 TDCATO>2.0.CO;2
- 623 Eggleston, S., & Galbraith, E. D. (2018). The devil's in the disequilibrium: Multi-  
624 component analysis of dissolved carbon and oxygen changes under a broad  
625 range of forcings in a general circulation model. *Biogeosciences*, 15(12), 3761–  
626 3777. doi: 10.5194/bg-15-3761-2018
- 627 Gloor, M., Gruber, N., Sarmiento, J., Sabine, C. L., Feely, R. A., & Rödenbeck, C.  
628 (2003). A first estimate of present and preindustrial air-sea CO<sub>2</sub> flux pat-  
629 terns based on ocean interior carbon measurements and models. *Geophysical*  
630 *Research Letters*, 30(1), 101–104. Retrieved from <http://doi.wiley.com/10.1029/2002GL015594> doi: 10.1029/2002GL015594
- 631 Groeskamp, S., Lenton, A., Matear, R., Sloyan, B. M., & Langlais, C. (2016). An-  
632 thropogenic carbon in the ocean—Surface to interior connections. *Global*  
633 *Biogeochemical Cycles*, 30(11), 1682–1698. Retrieved from <http://doi.wiley.com/10.1002/2016GB005476> doi: 10.1002/2016GB005476
- 634 Groeskamp, S., Zika, J. D., McDougall, T. J., Sloyan, B. M., & Laliberté, F. (2014).  
635 The Representation of Ocean Circulation and Variability in Thermodynamic  
636 Coordinates. *Journal of Physical Oceanography*, 44(7), 1735–1750. doi:  
637 10.1175/JPO-D-13-0213.1
- 638 Gruber, N., Gloor, M., Mikaloff Fletcher, S. E., Doney, S. C., Dutkiewicz, S., Fol-  
639 lows, M. J., ... Takahashi, T. (2009). Oceanic sources, sinks, and trans-  
640 port of atmospheric CO<sub>2</sub>. *Global Biogeochemical Cycles*, 23(1), 1–21. doi:  
641 10.1029/2008GB003349
- 642 Ito, T., & Follows, M. J. (2005). Preformed phosphate, soft tissue pump and  
643 atmospheric CO<sub>2</sub>. *Journal of Marine Research*, 63(4), 813–839. Re-  
644 trieved from <http://www.ingentaselect.com/rpsv/cgi-bin/cgi?ini=xref{\&}body=linker{\&}reqdoi=10.1357/0022240054663231> doi:  
645 10.1357/0022240054663231
- 646 Iudicone, D., Rodgers, K. B., Stendardo, I., Aumont, O., Madec, G., Bopp, L., ...  
647 Ribera D'Alcalá, M. (2011). Water masses as a unifying framework for under-  
648 standing the Southern Ocean Carbon Cycle. *Biogeosciences*, 8(5), 1031–1052.

652 doi: 10.5194/bg-8-1031-2011

- 653 Jones, C. D., Hughes, J. K., Bellouin, N., Hardiman, S. C., Jones, G. S., Knight,  
654 J., ... Zerroukat, M. (2011). The HadGEM2-ES implementation of CMIP5  
655 centennial simulations. *Geoscientific Model Development*, 4(3), 543–570. doi:  
656 10.5194/gmd-4-543-2011
- 657 Landschützer, P., Gruber, N., Haumann, F. A., Rödenbeck, C., Bakker, D. C. E.,  
658 van Heuven, S., ... Wanninkhof, R. (2015). The reinvigoration of the  
659 southern ocean carbon sink. *Science*, 349(6253), 1221–1224. Retrieved  
660 from <http://science.sciencemag.org/content/349/6253/1221> doi:  
661 10.1126/science.aab2620
- 662 Lauderdale, J. M., Garabato, A. C. N., Oliver, K. I. C., Follows, M. J., & Williams,  
663 R. G. (2013). Wind-driven changes in southern ocean residual circulation,  
664 ocean carbon reservoirs and atmospheric co<sub>2</sub>. *Climate dynamics*, 41(7-8),  
665 2145–2164.
- 666 Le Quéré, C., Rödenbeck, C., Buitenhuis, E. T., Conway, T. J., Langenfelds, R.,  
667 Gomez, A., ... Heimann, M. (2007). Saturation of the southern ocean co<sub>2</sub>  
668 sink due to recent climate change. *Science*, 316(5832), 1735–1738. Retrieved  
669 from <http://science.sciencemag.org/content/316/5832/1735> doi:  
670 10.1126/science.1136188
- 671 Levy, M., Bopp, L., Karleskind, P., Resplandy, L., Ethe, C., & Pinsard, F. (2013).  
672 Physical pathways for carbon transfers between the surface mixed layer and  
673 the ocean interior. *Global Biogeochemical Cycles*, 27(4), 1001-1012. Retrieved  
674 from <https://agupubs.onlinelibrary.wiley.com/doi/abs/10.1002/gbc.20092> doi: 10.1002/gbc.20092
- 675 Lewis, E., Wallace, D., & Allison, L. J. (1998). *Program developed for co<sub>2</sub> system*  
676 *calculations* (No. ORNL/CDIAC-105). Carbon Dioxide Information Analysis  
677 Center, managed by Lockheed Martin Energy Research Corporation for the US  
678 Department of Energy Tennessee.
- 679 Madec, G. (2012). NEMO ocean engine. *Note du Pôle de modélisation, Institut*  
680 *Pierre-Simon Laplace (IPSL)*(27), 357pp. Retrieved from <http://eprints.soton.ac.uk/64324/>
- 681 Marshall, J., & Speer, K. (2012, Mar 01). Closure of the meridional overturning  
682 circulation through southern ocean upwelling. *Nature Geoscience*, 5(3), 171-

- 685        180. Retrieved from <https://doi.org/10.1038/ngeo1391> doi: 10.1038/  
686        ngeo1391
- 687        McDougall, T. J., & Barker, P. M. (2011). Getting started with teos-10 and the  
688        gibbs seawater (gsw) oceanographic toolbox. *SCOR/IAPSO WG*, 127, 1–28.
- 689        Mikaloff Fletcher, S. E., Gruber, N., Jacobson, A. R., Gloor, M., Doney, S. C.,  
690        Dutkiewicz, S., ... Sarmiento, J. L. (2007). Inverse estimates of the oceanic  
691        sources and sinks of natural CO<sub>2</sub> and the implied oceanic carbon transport.  
692        *Global Biogeochemical Cycles*, 21(1), 1–19. doi: 10.1029/2006GB002751
- 693        Ödalen, M., Nylander, J., Oliver, K. I. C., Brodeau, L., & Ridgwell, A. (2018). The  
694        influence of the ocean circulation state on ocean carbon storage and co<sub>2</sub> draw-  
695        down potential in an earth system model. *Biogeosciences*, 15(5), 1367–1393.  
696        Retrieved from <http://www.biogeosciences.net/15/1367/2018/> doi:  
697        10.5194/bg-15-1367-2018
- 698        Raven, J., & Falkowski, P. (1999). Oceanic sinks for atmospheric co<sub>2</sub>. *Plant, Cell &*  
699        *Environment*, 22(6), 741–755.
- 700        Sabine, C. L., Feely, R. A., Gruber, N., Key, R. M., Lee, K., Bullister, J. L., ...  
701        Rios, A. F. (2004). The oceanic sink for anthropogenic co<sub>2</sub>. *Science*,  
702        305(5682), 367–371. Retrieved from <http://science.sciencemag.org/content/305/5682/367> doi: 10.1126/science.1097403
- 703        Sarmiento, J. L., & Gruber, N. (2006). *Ocean biogeochemical dynamics*. Princeton  
704        University Press.
- 705        Speer, K., Rintoul, S. R., & Sloyan, B. (2000). The Diabatic Deacon Cell\*.  
706        *Journal of Physical Oceanography*, 30(12), 3212–3222. Retrieved from  
707        [http://journals.ametsoc.org/doi/abs/10.1175/1520-0485\(2000\)030<3212:TDDC>2.0.CO;2](http://journals.ametsoc.org/doi/abs/10.1175/1520-0485(2000)030<3212:TDDC>2.0.CO;2) doi: 10.1175/  
708        1520-0485(2000)030<3212:TDDC>2.0.CO;2
- 709        Takahashi, T., Sutherland, S. C., Sweeney, C., Poisson, A., Metzl, N., Tilbrook,  
710        B., ... Nojiri, Y. (2002). Global sea-air CO<sub>2</sub> flux based on climatolog-  
711        ical surface ocean pCO<sub>2</sub>, and seasonal biological and temperature effects.  
712        *Deep Sea Research Part II: Topical Studies in Oceanography*, 49(9-10), 1601–  
713        1622. Retrieved from [https://doi.org/10.1016/S0967-0645\(02\)00003-6](https://doi.org/10.1016/S0967-0645(02)00003-6) doi: 10.1016/S0967-0645(02)00003-6
- 714
- 715
- 716
- 717

- Talley, L. D. (2013). Closure of the global overturning circulation through the indian, pacific, and southern oceans: Schematics and transports. *Oceanography*, 26. Retrieved from <https://doi.org/10.5670/oceanog.2013.07>

Timmermann, R., Goosse, H., Madec, G., Fichefet, T., Ethe, C., & Duli  re, V. (2005). On the representation of high latitude processes in the ORCA-LIM global coupled sea ice-ocean model. *Ocean Modelling*, 8(1-2), 175–201. doi: 10.1016/j.ocemod.2003.12.009

Volk, T., & Hoffert, M. I. (1985). Ocean carbon pumps: Analysis of relative strengths and efficiencies in ocean–driven atmospheric co<sub>2</sub> changes. In E. T. Sundquist & W. S. Broecker (Eds.), *The carbon cycle and atmospheric co<sub>2</sub>: Natural variations archean to present* (pp. 99–110). Washington D.C.: American Geophysical Union.

Volk, T., & Hoffert, M. I. (2013). Ocean carbon pumps: Analysis of relative strengths and efficiencies in ocean-driven atmospheric co<sub>2</sub> changes. In *The carbon cycle and atmospheric co<sub>2</sub>: Natural variations archean to present* (p. 99-110). American Geophysical Union (AGU). Retrieved from <https://agupubs.onlinelibrary.wiley.com/doi/abs/10.1029/GM032p0099> doi: 10.1029/GM032p0099

Weiss, R. (1974). Carbon dioxide in water and seawater: the solubility of a non-ideal gas. *Marine chemistry*, 2(3), 203–215.

Williams, R. G., & Follows, M. J. (2011). *Ocean Dynamics and the Carbon Cycle: Principles and mechanisms*. Cambridge: Cambridge University Press. Retrieved from <http://ebooks.cambridge.org/ref/id/CBO9780511977817> doi: 10.1017/CBO9780511977817

Yasunaka, S., Siswanto, E., Olsen, A., Hoppema, M., Watanabe, E., Fransson, A., ... Mathis, J. T. (2018). Arctic Ocean CO<sub>2</sub> uptake: an improved multiyear estimate of the air–sea CO<sub>2</sub> flux incorporating chlorophyll *a* concentrations. *Biogeosciences*, 15(6), 1643–1661. Retrieved from <https://www.biogeosciences.net/15/1643/2018/> doi: 10.5194/bg-15-1643-2018

Yool, A., Popova, E. E., & Anderson, T. R. (2013). MEDUSA-2.0: An intermediate complexity biogeochemical model of the marine carbon cycle for climate change and ocean acidification studies. *Geoscientific Model Development*, 6(5), 1767–1811. doi: 10.5194/gmd-6-1767-2013

- 751 Yool, A., Popova, E. E., & Coward, A. C. (2015). Future change in ocean productivity : Is the Arctic the new Atlantic? *Journal of Geophysical Research Oceans*,  
752 120, 7771–7790. doi: 10.1002/2015JC011167.Received  
753 Zika, J. D., England, M. H., & Sijp, W. P. (2012). The Ocean Circulation in Ther-  
754 mohaline Coordinates. *Journal of Physical Oceanography*, 42(5), 708–724. doi:  
755 10.1175/JPO-D-11-0139.1

Accepted Article